Heliyon 10 (2024) e27296

Contents lists available at ScienceDirect

Heliyon

journal homepage: www.cell.com/heliyon

Research article

Streamlined synthesis of iron and cobalt loaded MCM-48: High-performance heterogeneous catalysts for selective liquid-phase oxidation of toluene to benzaldehyde

Arnab Kalita *, Anup Kumar Talukdar

Department of Chemistry, Gauhati University, Gopinath Bordoloi Nagar, Jalukbari, Guwahati, Assam, 781014, India

ARTICLE INFO

Keywords:
Toluene
Benzaldehyde
Heterogeneous
Mesoporous

ABSTRACT

Hydrothermal synthesis of MCM-48 molecular sieves featuring the incorporation of both iron and cobalt with Si/M ratios of 20, 40 and 80 (where M represents either iron or cobalt) was performed using tetraethyl orthosilicate as the silica source and cetyltrimethylammonium bromide as a template. To gain a comprehensive understanding of the synthesized materials, these were thoroughly characterized using various techniques, including XRD, XPS, UV–Vis (DRS), FT-IR, N_2 adsorption-desorption analysis, SEM with EDX, TEM, TGA and NH_3-TPD analysis. XRD analysis revealed the presence of well-ordered MCM-48 structure in the metal-incorporated materials, while XPS and UV–Vis DRS confirmed the successful partial incorporation of metal ions precisely in their desired tetrahedral coordination within the framework. To assess their catalytic performance, we studied the activity and selectivity of these catalysts in liquid phase oxidation of toluene using *tert*-butyl hydroperoxide as the oxidant. Under optimized conditions, employing a 6% (w/w) Fe-MCM-48 (40) catalyst and maintaining a toluene to oxidant molar ratio of 1:3 at 353 K in a solvent-free environment for 8 h, the oxidation reaction resulted in the formation of benzaldehyde (88.1%) as the major product and benzyl alcohol (11.9%) as the minor product.

1. Introduction

Toluene, a volatile organic compound (VOC), poses environmental risks through industrial processes, consumer goods manufacturing and use. It contributes to terrestrial ozone formation [1], harming human health, crops and ecosystems. Improper disposal contaminates soil and water, endangering aquatic life. The EPA classifies toluene as a hazardous air pollutant (HAP). It is a significant source of urban air pollution from industries and vehicles, causing respiratory and neurological symptoms. Prolonged exposure damages the central nervous system, liver, kidneys and reproductive system [2,3]. World leaders and prominent scientists are, therefore, dedicated to implementing proactive strategies to regulate toluene emissions and promote eco-friendly alternatives. Numerous techniques, including adsorption [4,5], absorption [6], condensation [7], catalysis [8], bio-membrane separation [9,10], bio-destruction, thermal combustion [11,12], photocatalysis [13,14] and plasma [11,12], have been employed for VOC control, but they often demand fiddly and time-consuming processes, conflicting with the principles of green chemistry and technology.

The controlled oxidation of toluene yields benzaldehyde and benzyl alcohol, crucial compounds in industries like pharmaceuticals [15], perfumery, chemicals and plastics [16]. However, current methods involving chlorination followed by hydrolysis [17] pose

* Corresponding author..
E-mail addresses: arnabkalita26@gmail.com (A. Kalita), aktalukdar@gauhati.ac.in (A.K. Talukdar).

https://doi.org/10.1016/j.heliyon.2024.e27296
Received 18 August 2023; Received in revised form 23 February 2024; Accepted 27 February 2024
Available online 5 March 2024

challenges due to harsh reaction conditions, generation of toxic chlorinated waste detrimental to the environment and equipment, costly separation protocols and limited selectivity towards desired products [18]. Researchers have thus endeavoured to develop alternative catalytic routes for the oxidation of toluene under mild and environmentally friendly conditions [19].

Over the past few decades, significant progress has been made in synthesizing catalysts for the oxidation of toluene. Initially, focus was on homogeneous catalysts, such as metal complexes of copper, manganese and iron (III)-containing porphyrins, Schiff bases, tetraazaanulenes, chlorins and triazacyclononane ligands [20]. However, these catalysts have limitations including high cost, challenges associated with ligand synthesis, poor selectivity and limited recyclability, rendering them unsuitable for practical and industrial applications [21]. In order to alleviate such impediments, researches have turned to the synthesis of heterogeneous catalysts, which offer advantages such as facile recovery and separation of the catalyst [22–26], a straightforward synthesis process, enhanced recyclability and increased selectivity towards desired yields [27]. Moreover, heterogeneous catalysts offer an environmentally conscious approach to synthetic chemistry by curtailing the consumption of toxic and hazardous chemicals [28].

In the early 1990s, Kresge et al. at Mobil Oil Corporation achieved a significant milestone by successfully synthesizing a class of mesoporous materials known as M41S [29]. Since then, extensive research has been focused on porous materials for a wide range of applications [30,31]. Mesoporous silica-based materials, including MCM-41, MCM-48 and SBA-15 have garnered significant attention in heterogeneous catalysis due to their remarkable features such as high surface area, uniform pores with large diameters and excellent thermal stability [29]. Among these mesoporous materials, MCM-48 stands out as a particularly promising choice for catalytic applications, mainly due to its unique cubic arrangement and continuous three-dimensional interwoven structure, which effectively minimizes the likelihood of pore blockage by guest molecules [32–37].

While the parent siliceous materials showed promise, their catalytic activity was limited due to their framework neutrality. This prompted researchers to focus on developing modified mesoporous silica materials by incorporating various transition and inner transition metals like Ti, V, Cr, Mn and Ce either through framework substitution or as support [38–41]. These modified materials have demonstrated exceptional activity in a wide range of organic transformations including oxidation of aromatic and aliphatic hydrocarbons [42].

To boost the catalytic applications of the siliceous framework, enhancements were made to the inorganic wall compositions through the incorporation of heteroatoms. This strategic substitution of silicon with alternative elements allowed fine tuning of the framework's acidity and/or redox properties. The modification of the framework composition was accomplished through two distinct methodologies: the direct synthesis approach, involving a fusion of silicon and the desired heteroatom and the post-synthesis technique applied to existing silica mesoporous material. The direct synthesis method ensured a relatively even integration of the heteroatom, while the post-synthesis approach predominantly altered the surface of the walls, thereby promoting the heteroatom's concentration at the surface. In a previous study done in our lab, a thorough analysis of transition metal-modified MCM-48 revealed a noticeable improvement in the pore architecture with an increased mesopore volume and expanded pore diameter, surpassing those of the unmodified parent materials [43,44]. Iron and cobalt incorporation into MCM-48 have garnered substantial attention across multiple disciplines. The integration of Fe^{+3} ions into the cubic framework of MCM-48 presents intriguing prospects, as these ions exhibit remarkable sensitivity to oxidation-reduction reactions, thereby enhancing the catalyst's efficacy in oxidation processes [45]. Similarly, the presence of redox-active sites in Co incorporated MCM-48 materials grant them the opportunity to act as catalysts, actively participating in a diverse array of catalytic reactions [46].

Extensive scholarly investigations have been conducted over the past decades in the field of toluene oxidation utilizing porous materials as catalysts, accompanied by in-situ or surface modification of transition and inner transition metals, as a means to enhance catalytic efficiency sustainably. Notable contributions include Francisco et al., who incorporated iron oxides into a montmorillonite-rich raw-clay material, resulting in a catalyst sample with enhanced catalytic activity for toluene oxidation, but requiring a higher temperature for complete conversion [47]. Yunsheng et al. successfully synthesized mesoporous nickel oxide nanoparticles, achieving impressive conversion rates for toluene and formaldehyde, yet at elevated temperatures [48]. Influence of support morphology on catalytic activity was explored by Yuan et al., with rod-like SBA-15 support exhibiting the highest activity in toluene conversion [49]. Xingru et al. studied Pt–Pd/MCM-41 bimetallic catalysts and found superior performance compared to single metal catalysts [50]. Faiha et al. explored the use of mesoporous ferrisilicates as supports, with increased iron content and the presence of gold enhancing catalytic activity in toluene oxidation [51]. In another study, Douglas et al. successfully prepared copper zeolites by exchanging sodium in NaX zeolite with copper, creating a bifunctional material capable of both adsorption and catalytic oxidation of toluene at low temperatures. The copper zeolite with a low copper content exhibited promising toluene adsorption capacity and total oxidation properties [52]. Despite these advancements, limitations such as high temperatures and the production of deep or total oxidation products remain to be addressed for practical applications. In their study, Bendahou et al. synthesized lanthanum-substituted mesoporous SBA-15 molecular sieves using different methods and impregnated them with platinum or palladium. The catalytic activity for total toluene oxidation was observed best for 0.5 wt% Pd/SBA-15. The lower activity of the lanthanum-based catalysts may be attributed to the presence of LaO_X patches on the surface of the metal particles [53]. On the other hand, Hae et al. investigated the catalytic oxidation of toluene using ozone at room temperature, comparing various catalysts. Mesoporous $Mn/\gamma\text{-}Al_2O_3$ displayed highest catalytic activity and CO_2/CO ratio due to its larger surface area, weak $Mn–Al_2O_3$ interaction and higher Mn_2O_3 content [54]. However, by-product deposition and coking were a few limitations to consider. In their research, Narayanan et al. synthesized hexagonal cubic ZSM-5 zeolites using a hydrothermal method with surfactant-assisted mesopore templating, demonstrating good toluene conversion but limited selectivity towards benzaldehyde in liquid phase oxidation [55]. Meanwhile, Sreenivasulu et al. developed highly efficient solid acid catalysts for toluene oxidation by synthesizing titanium (IV) n-butoxide, achieving impressive toluene conversion and selectivity towards benzaldehyde [56]. However, the use of titanium (IV) n-butoxide as a precursor was expensive and potentially harmful to the eyes. Additionally, Nanli et al. synthesized bimodal mesoporous silica-supported Pd catalysts that

outperformed unimodal mesoporous silica-supported Pd catalysts in toluene oxidation [57]. He et al. synthesized MnO_x/HZSM-5 catalysts with varying manganese contents and discovered that the 10% MnO_x/HZSM-5 catalyst demonstrated optimal catalytic performance, high durability in dry conditions and efficient regeneration in humid conditions [58]. These studies highlight the advancements made in toluene oxidation, but also acknowledge the limitations of poor selectivity and the use of costly and toxic reagents. Nonetheless, the quest for reliable and efficient method for toluene oxidation remains in high demand.

In this current investigation, our primary objective entailed the synthesis through an in-situ modification methodology and subsequent characterization of MCM-48 materials incorporating iron and cobalt metals. Thereupon, we aimed to evaluate the catalytic performance of these synthesized materials for oxidation of toluene, employing *tert*-butyl hydroperoxide (TBHP) (70% w/v) as the oxidizing agent. (Scheme 1).

2. Experimental

2.1. Source of chemicals

The chemicals applied for the synthesis of MCM-48 and modified MCM-48 materials included tetraethyl orthosilicate (Sigma Aldrich, purity: 98%), absolute alcohol (A.K. Sales Agency, purity: 99.9%), cetyltrimethylammonium bromide (Sigma Aldrich, minimum purity: 98%), aqueous ammonia (Merck, concentration: 25%), ferric nitrate nonahydrate (Sigma Aldrich, minimum purity: 98%) and cobaltous nitrate hexahydrate (Sigma Aldrich, minimum purity: 98%). These chemicals and reagents were procured from commercial sources and were utilized without the need for additional purification. The synthesis procedure involved the use of double distilled water.

2.2. Synthesis of parent and modified MCM-48

Tetraethyl orthosilicate (TEOS) was the primary silica source used in this investigation and Si-MCM-48 was synthesized in a single step utilizing a previously published innovative approach done in our lab by Kalita et al. [43]. The necessary raw materials were combined in a solution that included 2.8 g of cetyltrimethylammonium bromide (CTAB) dissolved in 135 ml of distilled water and the mixture was subjected to stirring for a duration of 20 min. While continuously stirring the solution with a mechanical stirrer for 2 h, 4 g of TEOS were gradually added drop by drop. Following the 2-h stirring period, the resulting solution was subjected to autoclaving at a temperature of 393 K for 6 h. Subsequently, a solid product was obtained and separated from the mother liquor through a simple filtration process using filter papers with a pore diameter of 110 mm. The pH of the solid product was maintained at neutral by continuous washing with distilled water. The resulting solid product was then air-dried at room temperature, followed by a drying period of 6 h at 393 K. Finally, the dried product underwent calcination in a programmable furnace at a temperature of 813 K for a duration of 5 h. The molar gel composition was TEOS: NH_3: EtOH: CTAB: H_2O = 1: 13: 56: 0.4: 405.

Synthesis of metal loaded MCM-48 was carried out using the identical plan of action with the proviso that the metal sources were added after the addition of silica source [59]. A string of MCM-48 incorporating cobalt and iron were synthesized by altering the molar ratio of silicon to metal in the synthesis coagulate. Table 1 presents the names of the synthesized samples, including the parent material and metal-incorporated MCM-48, along with their corresponding molar ratios and mol-gel compositions. The molar gel composition was TEOS: M: NH_3: EtOH: CTAB: H_2O = 1: X: 13: 56: 0.4: 405, where X = 20, 40 and 80 respectively.

2.3. General procedure for oxidation of toluene

The experimental procedure involved conducting reactions in a 25 ml round-bottom flask equipped with a reflux condenser, placed on a magnetic stirrer under atmospheric pressure and regulated for temperature. In a standard reaction, a quantity of X moles of toluene and Y moles of *tert*-butyl hydroperoxide (70% w/v) were reacted with W grams of the prepared samples in a solvent-free environment, with continuous stirring. Prior to use in the reaction mixture, the prepared samples were activated by heating them at 120 °C for 1 h each time. The influence of various reaction parameters, such as reaction time, temperature, molar ratio of reactant and oxidant, metal loadings, quantity of catalysts, the effect of different solvents and the impact of different substituent groups on the parent substrate were studied. The products, along with the any unreacted reactants, were collected at different time intervals and subjected to gas chromatography analysis to determine the conversion percentage and selectivity of the products. The conversion of the reactant and selectivity of the products were calculated using the following equation:

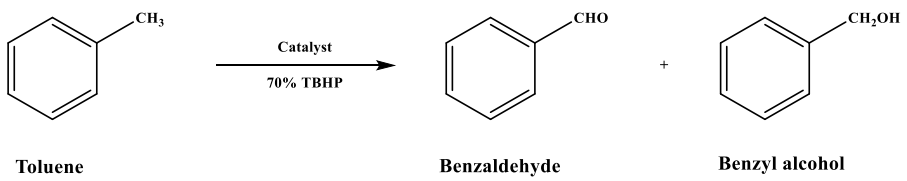

Scheme 1. Oxidation of toluene to benzaldehyde and benzyl alcohol.

Table 1
Designation, molar ratio and molar gel composition of parent and modified MCM-48 samples.

Entry	Designations	Molar ratio (Si/metal)	Molar gel composition (TEOS: M: NH_3: EtOH: CTAB: H_2O)
1	Si-MCM-48	–	1: 0: 13: 56: 0.4: 405
2	Fe-MCM-48 (20)	20	1: 20: 13: 56: 0.4: 405
3	Fe-MCM-48 (40)	40	1: 40: 13: 56: 0.4: 405
4	Fe-MCM-48 (80)	80	1: 80: 13: 56: 0.4: 405
5	Co-MCM-48 (20)	20	1: 20: 13: 56: 0.4: 405
6	Co-MCM-48 (40)	40	1: 40: 13: 56: 0.4: 405
7	Co-MCM-48 (80)	80	1: 80: 13: 56: 0.4: 405

$$\text{Conversion}(\%) = \left[\frac{(\text{toluene})_0 - (\text{toluene})_t}{(\text{toluene})_0}\right] \times 100$$

$$\text{Selectivity}\left(\%\right) = \left[\frac{\text{moles of desired products}}{\text{moles of all the products}}\right] \times 100$$

$(\text{toluene})_0$ = initial concentration of toluene
$(\text{toluene})_t$ = concentration of toluene at time t

2.4. Characterization of the synthesized materials

In order to identify the mesophase of the calcined MCM-48 materials, X-ray diffraction (XRD) analysis was performed. The measurements encompassed recording powder XRD patterns in the 2Θ range of 2°–10°, as well as wide-angle XRD in the range of 5°–80°, employing a Rigaku Ultima IV instrument with CuKα (λ = 1.54 Å) radiation at room temperature. The oxidation states of metal centres within the framework of MCM-48 samples were analysed using X-ray photoelectron spectroscopy (XPS) with the Thermo Fisher Scientific's ESCALAB Xi + spectrometer. Diffuse reflectance UV–Vis (DRS) spectra were collected for the calcined samples using a Hitachi 4100 spectrometer. The spectra covered the range of 200–800 nm and baseline correction was performed using barium sulphate as the reference material. For infrared analysis, the IR spectra of the calcined MCM-48 materials were obtained in the form of KBr pellets using an IR Afinity-1 (SHIMADZU) spectrometer. The spectra were recorded in the mid-IR region of 4000-450 cm^{-1} with a resolution of 8 cm^{-1}. To characterize the textural properties of the samples, including surface area, pore size and pore volume, N_2 adsorption-desorption measurements were conducted. Isotherms of the calcined samples were obtained using a Micromeritics Tristar 3000 analyser, employing nitrogen as the adsorbate at a temperature of 77.15 K. To examine the morphology and elemental composition of the synthesized samples, scanning electron microscopy (SEM) and energy dispersive X-ray spectroscopic (EDX) analysis were conducted. The morphology was visualized using a Zeiss SIGMA 300 scanning electron microscope. A JEM-2100 Plus Electron Microscope operated at 200 kV was employed to conduct transmission electron microscopy (TEM) measurements on the samples. TGA analysis was performed on both the uncalcined and calcined MCM-48 samples, including both the parent and modified samples. The analysis was conducted using a Mettler Toledo TGA/DSC 1 STARe System analyser. The temperature range of 313–1013 K was covered with a heating rate of 7 K/min. The measurements were carried out under an inert N_2 gas atmosphere. NH_3-temperature programmed desorption (TPD) analysis of the calcined parent and modified samples was performed using Catalyst Analyser BELCAT II

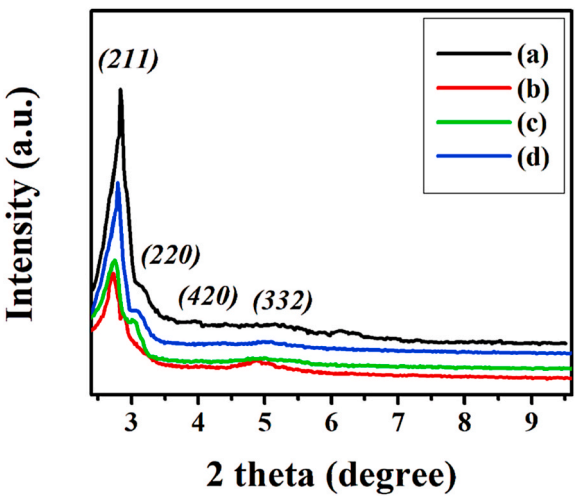

Fig. 1. Low-angle XRD plots of (a) Si-MCM-48, (b) Fe-MCM-48 (20), (c) Fe-MCM-48 (40), (d) Fe-MCM-48 (80).

chemisorption instrument in an inert helium atmosphere. Qualitative identification of the oxidative products was done by utilizing a PerkinElmer Clarus 600 gas chromatograph equipped with a PerkinElmer Clarus 600C mass spectrometer. Quantitative analysis of the products was performed by using a PerkinElmer Clarus 500 gas chromatograph equipped with an Elite-1 series column and a flame ionization detector (FID).

3. Results and discussion

3.1. X-ray diffraction analysis

The X-ray diffraction (XRD) patterns of the calcined Si-MCM-48 sample at low angles exhibit excellent conformity with those previously reported for cubic MCM-48 materials. In Fig. 1, we present the low-angle XRD patterns comparing the calcined Si-MCM-48 and Fe-MCM-48 and in Fig. 2, the low-angle XRD peaks of calcined Si-MCM-48 and Co-MCM-48 are shown. The diffraction peaks observed at approximately 2.8°, 3.2°, 4.3° and 5.2° in the parent MCM-48 sample can be assigned to the crystallographic planes *(2 1 1), (2 2 0), (4 2 0)* and *(3 3 2)* respectively [60]. This unequivocally demonstrates the formation of a well-ordered, long-range Ia3d cubic mesoporous framework [29]. Notably, both Fe-MCM-48 and Co-MCM-48 samples exhibit similar low-angle XRD patterns to that of the MCM-48 sample, indicating that the incorporation of Fe and Co into the MCM-48 framework maintains the cubic Ia3d mesoporous structure. Upon the incorporation of metal ions into the MCM-48 matrix, a visible downshift in the 2Θ values of the principal diffraction peaks is observed in comparison to the parent MCM-48 specimen. Furthermore, as the metal content increases, a decline in the observed intensity of the dominant diffraction peak *(2 1 1)* and its associated shoulder peak *(2 2 0)* is evident in both the Fe-MCM-48 and Co-MCM-48 samples. The observed phenomenon can be explained by the growing strain on the bonds and the greater number of defect sites that emerge when a heteroatom replaces silicon in the mesoporous structure of MCM-48 [59,61–63]. Using the appropriate equation, $a_0 = d_{211} \times (h^2+k^2+l^2)^{1/2}$, we calculated the cell parameter for each sample. Table 2 presents the d-spacing and corresponding cubic unit cell parameters (a_0) for the *(2 1 1)* reflection. Consistently, both the cubic unit cell parameters and d-spacing values demonstrate a progressive increase as the metal content in the sample rises. This observation suggests that the unit cell parameter expands with the inclusion of Fe^{3+} and Co^{2+} ions (ionic radius, 0.63 Å and 0.76 Å respectively), likely due to their larger size compared to Si^{4+} (0.40 Å). This expansion indicates the partial incorporation of iron and cobalt ions into the MCM-48 mesoporous molecular sieve framework. Similar findings were noted by earlier researchers when introducing different metal ions into MCM-48 [59,62,64,65].

Moreover, Figs. 1–3 (supplementary materials) display the wide-angle XRD patterns of Si-MCM-48, Fe-MCM-48 and Co-MCM-48 respectively. For a more in-depth discussion, please refer to the supplementary materials.

3.2. XPS analysis

To delve into chemical states of iron and cobalt in Fe-MCM-48 and Co-MCM-48 samples respectively, an analysis was conducted using XPS on the prepared samples. In the spectrum of Fe 2p for Fe-MCM-48 samples, two primary peaks appeared at around 711.6 eV and 725.1 eV (Fig. 3 (a), (b)), exhibiting an orbital splitting of approximately 13.5 eV. These peaks were attributed to Fe $2p_{3/2}$ and Fe $2p_{1/2}$ of Fe^{3+} respectively [66,67]. Moreover, satellite peaks at 716.5 and 733.4 eV are seen. In contrast to Fe_2O_3 (710.7 and 724.3 eV for $2p_{3/2}$ and $2p_{1/2}$, respectively), the Fe 2p signals exhibited a noticeable shift towards higher binding energies. This shift suggests that Fe^{3+} was not present in the oxide form but instead replaced Si^{4+}, forming Si–*O*–Fe bonds [67,68].

In the spectrum of Co 2p for Co-MCM-48 samples, the presence of peaks at 781.0 eV and 796.9 eV (Fig. 4 (a), (b) and (c)) signifies the Co $2p_{3/2}$ and Co $2p_{1/2}$ respectively. Furthermore, corresponding satellite peaks at 785.4 eV and 802.9 eV are observable. Upon

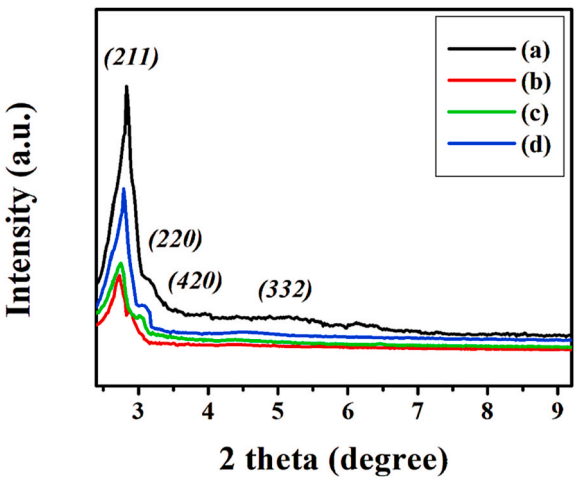

Fig. 2. Low-angle XRD plots of (a) Si-MCM-48, (b) Co-MCM-48 (20), (c) Co-MCM (40), (d) Co-MCM-48 (80).

Table 2
Crystallographic analysis data of [Si, Fe and Co] MCM-48 samples.

Entry	Samples	d spacing (Å) *d (211)*	a_0 (Å)
1	Si-MCM-48	31.30	76.66
2	Fe-MCM-48 (20)	32.33	79.19
3	Fe-MCM-48 (40)	32.10	78.62
4	Fe-MCM-48 (80)	31.75	77.77
5	Co-MCM-48 (20)	32.69	80.07
6	Co-MCM-48 (40)	32.45	79.48
7	Co-MCM-48 (80)	32.21	78.89

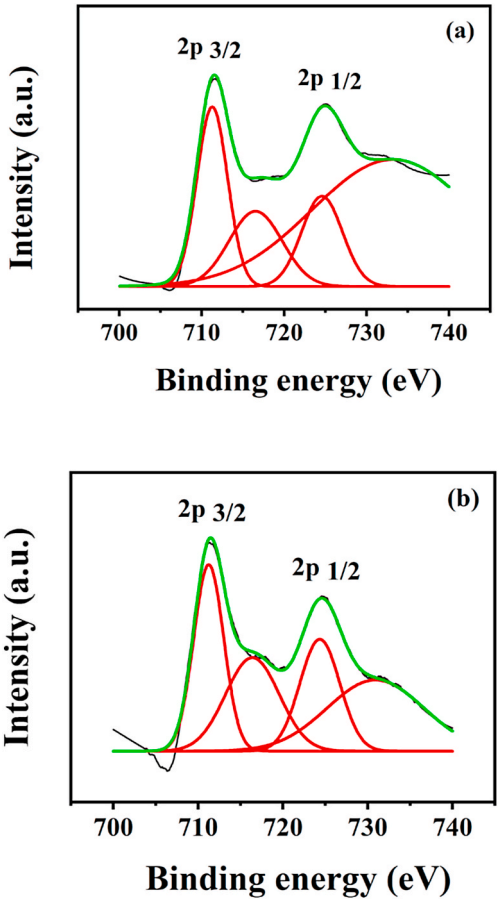

Fig. 3. X-ray photoelectron spectra (XPS) of (a) Fe-MCM-48 (20), (b) Fe-MCM-48 (80).

calculation, it was determined that the orbital splitting between the Co $2p_{1/2}$ and Co $2p_{3/2}$ peaks in these samples is approximately 16.0 eV, indicative of framework Co^{2+} species, as opposed to Co^{3+} compounds with a splitting value of 15.0 eV [69–71].

3.3. UV–vis DRS spectroscopic analysis

Upon examining the UV–Vis DRS spectra of the calcined MCM-48 samples enriched with Fe, a captivating observation emerges where two distinct absorption bands capture our attention, each holding its own significance (Fig. 5). The first band, prominently positioned within the 200–300 nm range, arises as a result of charge-transfer (CT) transitions orchestrated by solitary Fe^{3+} ions assuming a tetrahedral FeO_4^- geometry within the framework [59,65,72]. As we venture further into the spectrum, another broad absorption band unfolds, residing within the 300–600 nm range. This broad band is an ensemble of d-d transitions, performed by octahedral Fe^{3+} ions that have gathered together in tiny clusters [59,65,72].

Fig. 6 unveils an alluring feature for the Co loaded MCM-48 samples, a broad band stretching across the 480–550 nm range. This broad band signifies the presence of Co ions nestled in a tetrahedral arrangement within the silica framework [73–75]. Additionally,

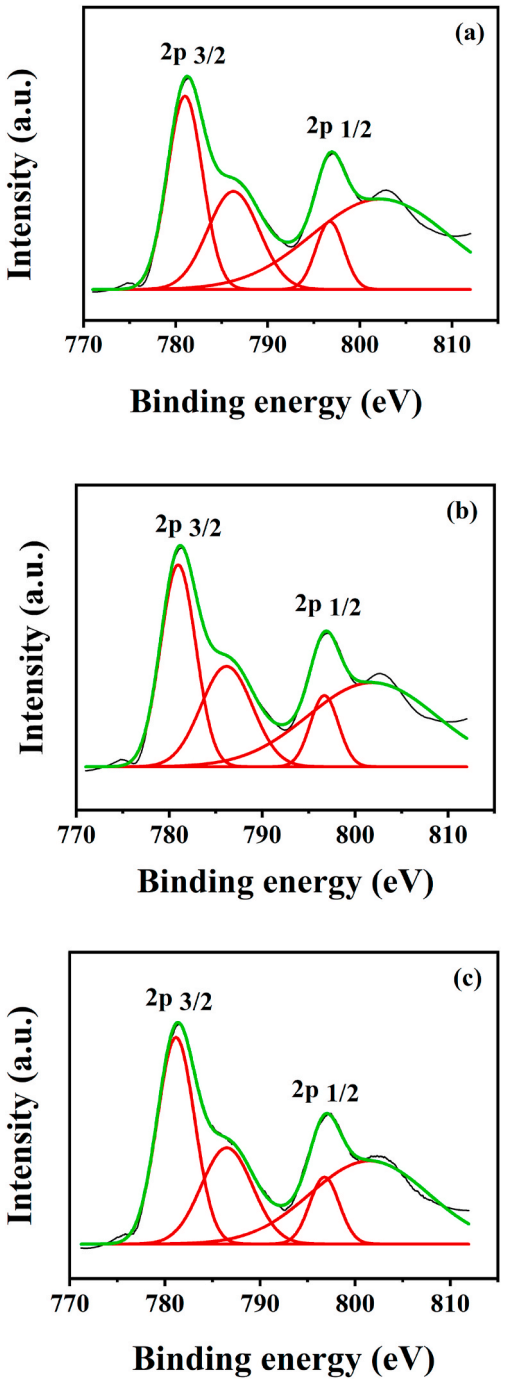

Fig. 4. X-ray photoelectron spectra (XPS) of (a) Co-MCM-48 (20), (b) Co-MCM-48 (40), (c) Co-MCM-48 (80).

peaks appearing around 330–400 nm indicate the presence of mixed oxides of cobalt, where cobalt exists in both tetrahedral and octahedral environments [92]. Moreover, observed peaks at approximately 250 nm are attributed to the oxygen-to-metal charge transfer transition [93]. The intensity of the adsorptive peaks within the Co-MCM-48 samples exhibit a gradual ascent, aligning with the increasing cobalt content within each sample. This revelation serves as another compelling piece of evidence, affirming the successful integration of cobalt into the MCM-48 structure.

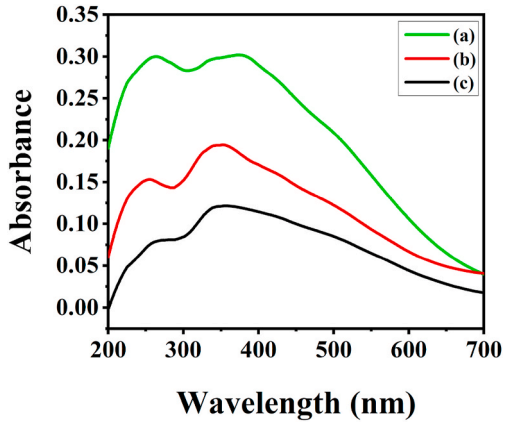

Fig. 5. UV–Vis DRS spectra of (a) Fe-MCM-48 (20), (b) Fe-MCM-48 (40), (c) Fe-MCM-48 (80).

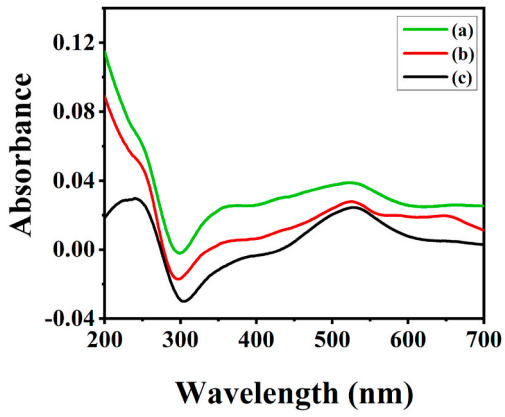

Fig. 6. UV–Vis DRS spectra of (a) Co-MCM-48 (20), (b) Co-MCM-48 (40), (c) Co-MCM-48 (80).

3.4. IR spectroscopic analysis

Figs. 7 and 8 present the IR spectra of Si-MCM-48 in comparison with those of all the MCM-48 samples loaded with iron and cobalt respectively. The broad band that emerges in the region of 3432 cm^{-1} in the FTIR spectra of the calcined parent, iron and cobalt

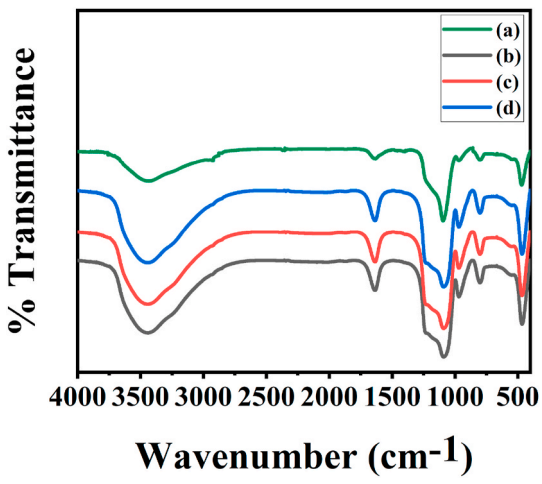

Fig. 7. IR spectra of (a) Si-MCM-48, (b) Fe-MCM-48 (20), (c) Fe-MCM-48 (40), (d) Fe-MCM-48 (80).

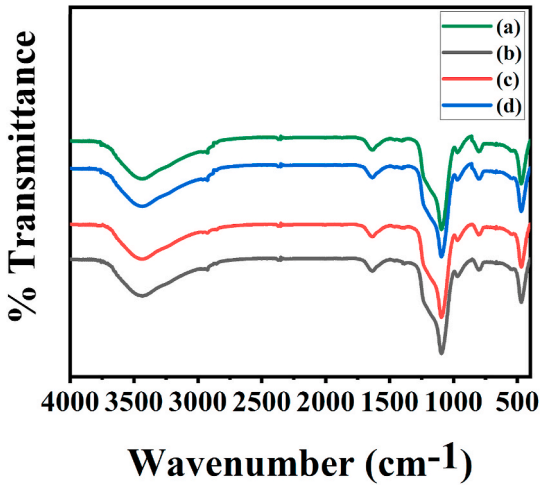

Fig. 8. IR spectra of (a) Si-MCM-48, (b) Co-MCM-48 (20), (c) Co-MCM-48 (40), (d) Co-MCM-48 (80).

modified MCM-48 samples is the classic OH stretching vibration, while the OH bending vibration appears at 1631 cm^{-1}. The presence of adsorbed water in these materials was established by the development of these two bands [76]. Bands at 802 cm^{-1} and 468 cm^{-1} are attributed to symmetric stretching and asymmetric bending of Si–*O*–Si bonds, respectively, while the broad band around 1081 cm^{-1} with a shoulder at 1240 cm^{-1} is associated with internal and external asymmetric Si–*O*–Si stretching vibration [77–79]. This investigation signifies the presence of compacted silica network in the prepared samples. Along with these peaks, a band with a centre at 961 cm^{-1} is seen in all of the spectra and is frequently attributed to vibration because of Fe–*O*–Si and Co–*O*–Si bonding in iron and cobalt containing zeolites respectively [80,81]. Since the spectra of pure silica MCM-48 also demonstrates the band, the assignment of this band to the Si–*O*-M (where M = Fe and Co) does not seem to be evident in the case of metal loaded mesoporous silicates. Based on this finding, it can be deduced that the vibrations of the M-*O*-Si bonds and the Si–OH groups overlap to cause the band to appear at 961 cm^{-1} [44].

3.5. N_2 adsorption-desorption analysis

The N_2 adsorption-desorption isotherms for MCM-48 and metal loaded samples, depicted in Figs. 9–11 respectively, were acquired by plotting the quantity of physiosorbed nitrogen against the relative pressure of the samples. In accordance with the IUPAC classification, these isotherms exhibit the characteristic features of a type IV isotherm, accompanied by an H3 hysteresis loop, thus signifying their association with highly ordered mesoporous materials. A distinguishable transition point, manifesting as a pronounced infection, is observed within the relative pressure range of 0.2–0.4. This distinct occurrence serves as a compelling indication of capillary condensation phenomenon, in which nitrogen undergoes condensation within the uniform pores of the material [59,65,82]. Fig. 12 presents the pore size distribution curves for the examined samples. Notably, these distribution curves exhibit a remarkably narrow pore size distribution, as observed uniformly across all samples. This observation highlights the exquisite precision and homogeneity of the pore dimensions within the studied materials. For a comprehensive understanding of the textural properties, we present an

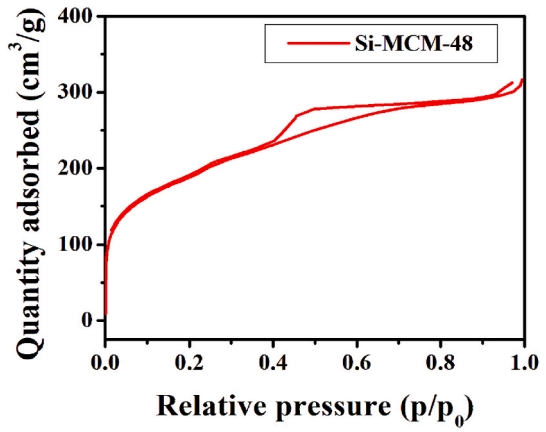

Fig. 9. Nitrogen adsorption-desorption isotherm of Si-MCM-48.

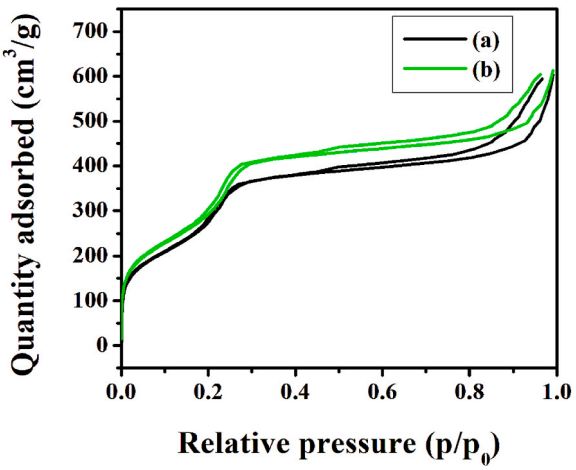

Fig. 10. Nitrogen adsorption-desorption isotherms of (a) Fe-MCM-48 (20), (b) Fe-MCM-48 (40).

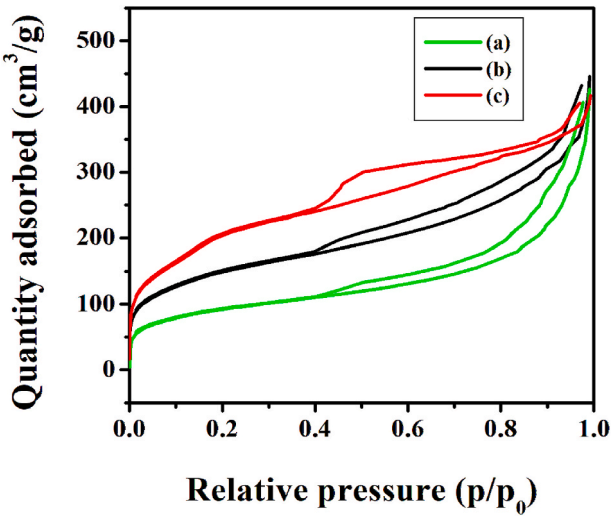

Fig. 11. Nitrogen adsorption-desorption isotherms of (a) Co-MCM-48 (20), (b) Co-MCM-48 (40), (c) Co-MCM-48 (80).

overview of the BET surface area (A_{BET}), mesopore diameter (D_{BJH}) and cumulative pore volume (V_{BJH}). These properties have been meticulously calculated using BET and BJH methods. A concise summary of these findings can be found in Table 3, enriching our comprehension of the intricate characteristics inherent to N_2 adsorption-desorption isotherms and the associated porous material system.

Observations reveal an increase in pore size when comparing the metal loaded samples to the parent Si-MCM-48. Additionally, a positive correlation is observed between pore size and the metal content, as evidenced by the data presented in Table 3. This notable variation in the pore size can potentially be attributed to the incorporation of heteroatoms into the mesoporous structure's framework, which is supported by the observed increase in the lattice parameter (a_0) values obtained from XRD analysis (Table 2). Interestingly, a noteworthy observation emerges as the metal content increases, showcasing a decrease in pore volume across all samples. This phenomenon suggests that the presence of occluded nano clusters of metal oxide within the pores could be the underlying cause for this reduction [43,44]. It is plausible that these nano clusters form as a result of the experimental conditions employed during the study. The occlusion of these metal oxide clusters within the pore spaces potentially leads to a constriction of the available volume for gas or fluid adsorption. Furthermore, study reveals distinct trends in the surface area of the parent Si-MCM-48 sample when compared to iron and cobalt loaded samples. Specifically, the iron loaded samples exhibit an increase in surface area, while the cobalt loaded samples demonstrate a decrease. Moreover, in case of Fe and Co loaded MCM-48, as the metal content increases, a reduction in surface area is observed.

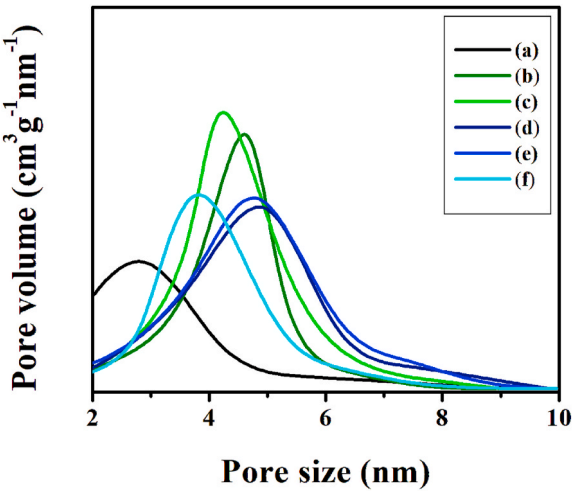

Fig. 12. Pore size distribution curves of (a) Si-MCM-48, (b) Fe-MCM-48 (20), (c) Fe-MCM-48 (40), (d) Co-MCM-48 (20), (e) Co-MCM-48 (40), (f) Co-MCM-48 (80).

Table 3
Textural properties of various samples.

Entry	Samples	Surface area A_{BET} (m^2/g)	Pore volume V_{BJH} (cm^3/g)	Pore size D_{BJH} (nm)
1	Si-MCM-48	675	0.48	2.84
2	Fe-MCM-48 (20)	784	0.92	4.69
3	Fe-MCM-48 (40)	910	0.94	4.14
4	Co-MCM-48 (20)	332	0.62	4.99
5	Co-MCM-48 (40)	541	0.65	4.81
6	Co-MCM-48 (80)	655	0.68	3.81

3.6. SEM and EDX analysis

Scanning electron microscopy (SEM) was employed to examine the particle morphology and size of both parent MCM-48 and metal incorporated MCM-48 samples. The obtained SEM images, displayed in Fig. 13 (a) to 13 (g), vividly illustrate that all particles exhibit a spherical configuration, exhibiting dimensions within the range of 300–600 nm. Additionally, the SEM micrographs revealed the presence of limited agglomerated crystalline structures within the samples [59].

In order to assess the presence of heteroatoms in the mesoporous silica materials, an analysis utilizing energy dispersive X-ray (EDX) was conducted. Please refer to supplementary materials for more details.

3.7. Transmission electron microscopy

Fig. 14 (a) to 14 (f) exhibit TEM images of Fe-MCM-48 and Co-MCM-48 samples taken along the cubic (*2 1 1*) planes. These images depict a three-dimensional cubic pore structure with long-range order, closely resembling the characteristic structure of typical MCM-48 material. This observation serves to confirm that the incorporation of iron and cobalt does not bring any noticeable changes. Additionally, the determined d-spacing and pore size values align consistently with the results obtained from both powder XRD and nitrogen sorption analysis [83–86].

3.8. Thermogravimetric analysis

The thermogravimetric analysis (TGA) plots of the uncalcined and calcined MCM-48 samples, both with and without the incorporation of iron and cobalt, are depicted in Figs. 6 and 7 (supplementary materials). For a deeper understanding, please refer to the supplementary materials.

3.9. NH_3-TPD analysis

NH_3-TPD analysis was employed to determine the acid sites distribution in Si-MCM-48, Fe-MCM-48 and Co-MCM-48 samples. A low-temperature desorption peak indicates weak acid sites, while a high-temperature desorption peak suggests strong acid sites. Si-MCM-48 exhibited very weakly intense desorption peaks at both temperatures, implying a lack of acid sites (Fig. 8, supplementary

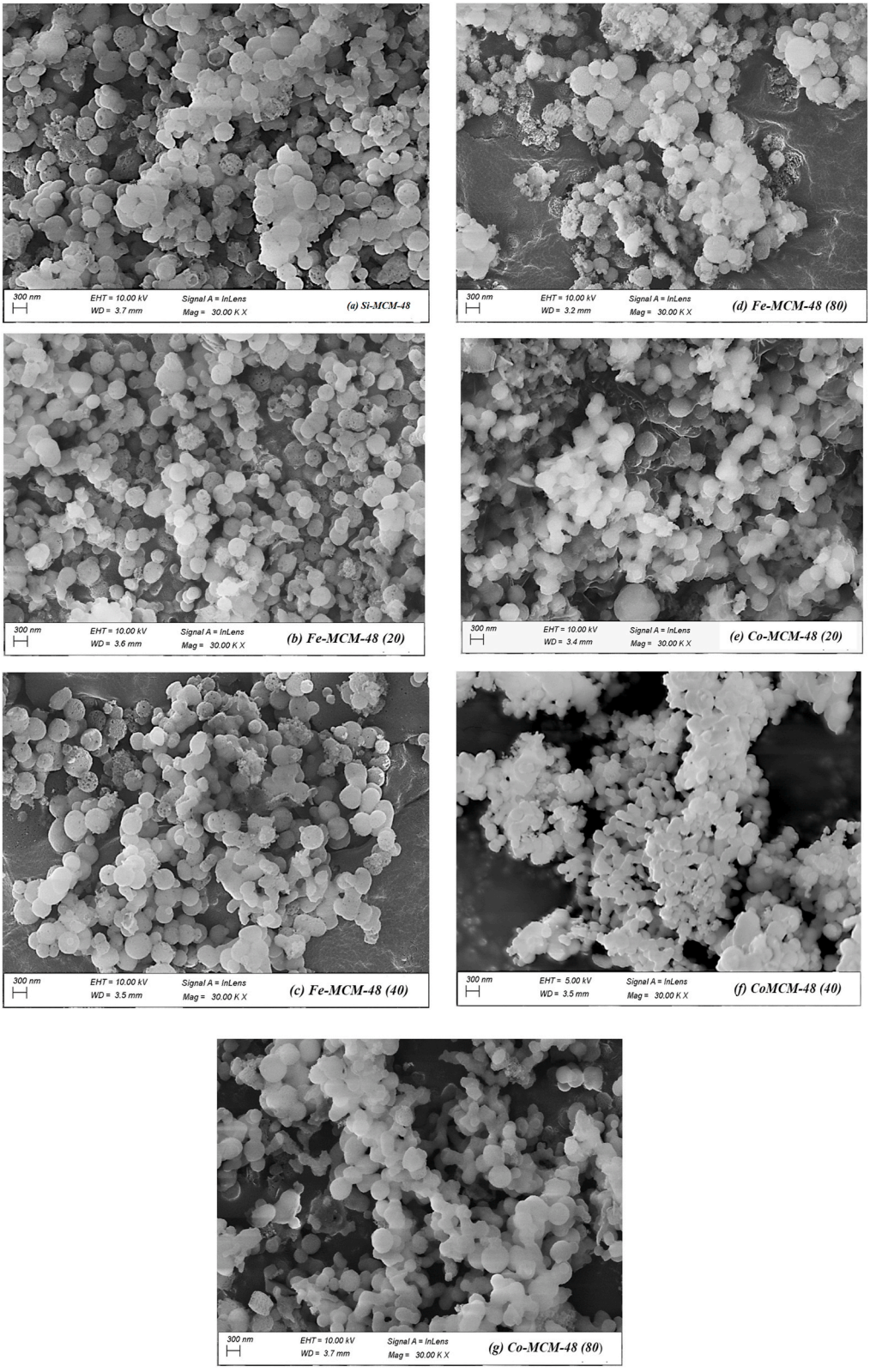

Fig. 13. SEM images of (a) Si-MCM-48, (b) Fe-MCM-48 (20), (c) Fe-MCM-48 (40), (d) Fe-MCM-48 (80), (e) Co-MCM-48 (20), (f) Co-MCM-48 (40) and (g) Co-MCM-48 (80).

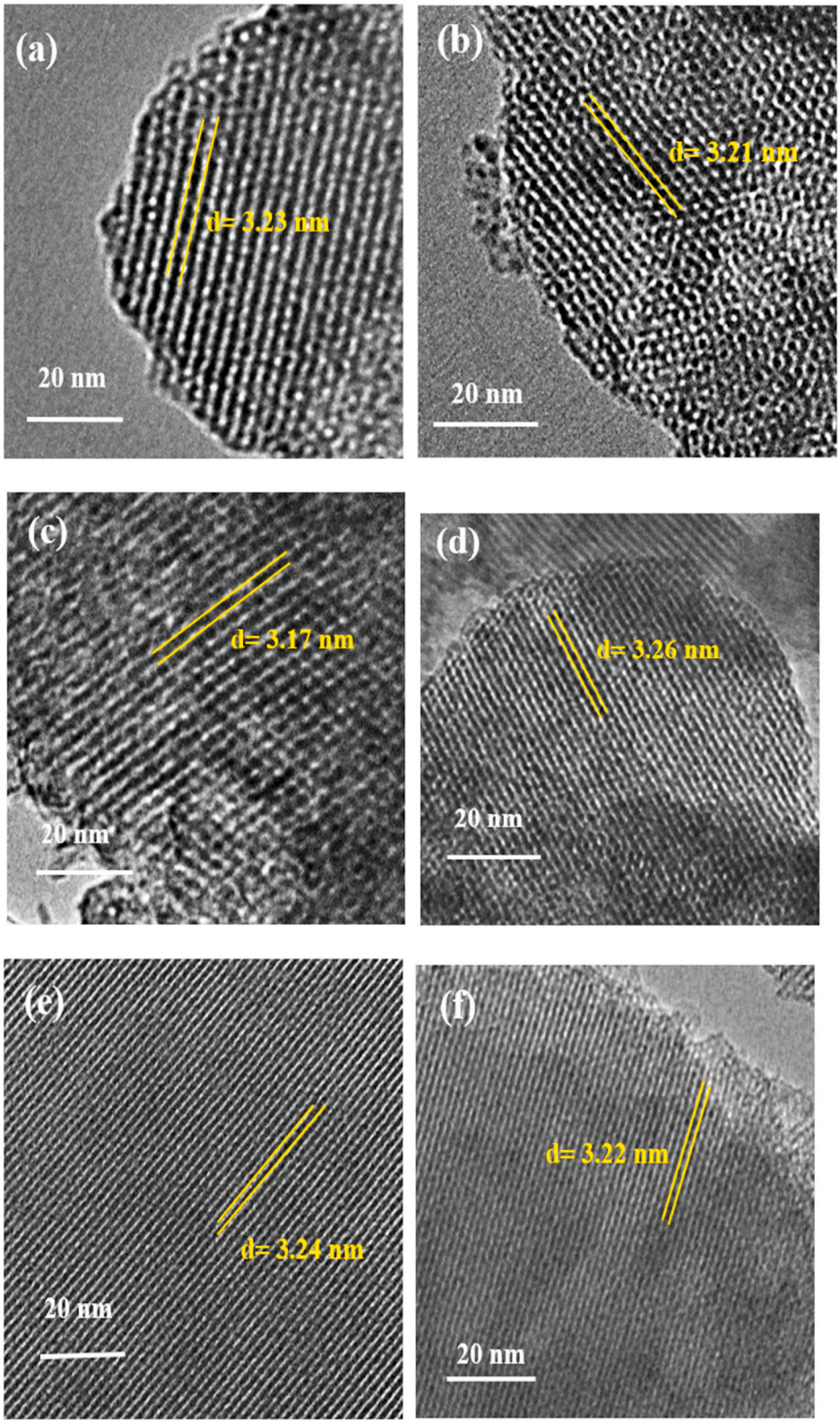

Fig. 14. TEM images of (a) Fe-MCM-48 (20), (b) Fe-MCM-48 (40), (c) Fe-MCM-48 (80), (d) Co-MCM-48 (20), (e) Co-MCM-48 (40), (f) Co-MCM-48 (80).

materials). Conversely, Fe and Co modified MCM-48 displayed two distinct desorption peaks (Figs. 15 and 16 respectively). The peak centred around 200 °C signified weak acid sites, while the peak above 350 °C indicated strong acid sites. At temperatures exceeding 350 °C, silanol groups undergo dihydroxylation accompanied by the release of water, leading to the potential formation of Lewis acid centres. This demonstrates that the modified MCM-48 gained acidity compared to parent material upon metal incorporation into the framework. Additionally, as the metal content increased, the intensity of the peaks also increased, suggesting a strengthening of the acid sites.

4. Catalytic activities

The catalytic properties of Fe and Co loaded MCM-48 samples for liquid phase oxidation of toluene was evaluated under various conditions. The reaction was conducted in a 25 mL two-necked round-bottom flask, fitted with a reflux condenser and a thermometer and was put in a temperature-controlled magnetic stirrer at 600 rpm. The reaction was initiated by introducing different amounts (in mL) of toluene with 70% w/v of *tert*-butyl hydroperoxide as the oxidizing agent in a solvent free environment under different temperatures and atmospheric pressure. MCM-48 embedded metal catalysts having tetrahedral geometry has been shown to be a more efficient catalysts in oxidation reaction compared to bare MCM-48 [42,43,45,46]. All the prepared Fe^{3+}/Co^{2+} ions incorporated MCM-48 samples also demonstrated enhanced activity in oxidation reaction compared to original MCM-48, which is attributed to the incorporation of Fe^{3+}/Co^{2+} ions in the tetrahedral framework of MCM-48. Optimal conditions for converting toluene were determined by manipulating various factors including metal loadings, reaction time, temperature, substrate to oxidant molar ratio, catalyst quantity, solvent influence and different substrate varieties. Product identification was done through the utilization of GC-MS (Fig. 9, supplementary materials). The conversion rate and selectivity of reaction products were assessed via gas chromatography. Remarkably, this reaction yielded two significant products, benzaldehyde and benzyl alcohol (Scheme 1) which had previously been documented in limited yields by other researchers [87–91].

4.1. Effect of metal loading on toluene oxidation

Fig. 17 shows the graphical results comparing the percentage of conversion and product selectivity for different metal-loaded MCM-48 catalysts in toluene oxidation reaction. XRD, N_2 adsorption-desorption and TEM analyses confirmed the incorporation of metal ions by observing increased d-spacing and pore diameter values. Interestingly, the iron-incorporated MCM-48 catalysts exhibited significantly higher conversion rates compared to the cobalt-incorporated ones under similar reaction conditions. This disparity can be attributed to the higher reduction potential of Fe^{+3} compared to Co^{+2}, which indicates a greater affinity for accepting electrons and facilitating the oxidation reaction. Moreover, iron in a tetrahedral environment within the MCM-48 framework provides the essential conditions that encourages stronger interaction and activation of toluene molecules, resulting in an increased catalytic activity. Among the iron-loaded catalysts, MCM-48 with a Si/Fe ratio of 40 demonstrated the highest conversion (86.7%) and selectivity (88.1%) towards benzaldehyde. This exceptional performance can be attributed to a balanced presence of redox active sites and an optimal surface area. Furthermore, varying the Si/M (M = Fe, Co) ratio from 80 to 40 and then to 20 (increasing metal content) initially increased conversion from 79.5% to 86.7%, followed by a decrease to 82.3% for iron, while for cobalt, it increased from 75.8% to 78.1% and then decreased to 77.4%. Notably, Si-MCM-48 exhibited low activity due to lack of active species promoting toluene oxidation. Consequently, Fe-MCM-48 (40) emerged as the optimized catalyst for ensuing studies.

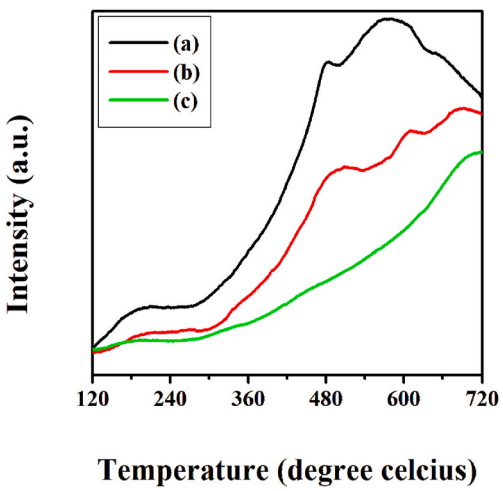

Fig. 15. NH_3-TPD profiles of (a) Fe-MCM-48 (20), (b) Fe-MCM-48 (40), (c) Fe-MCM-48 (80).

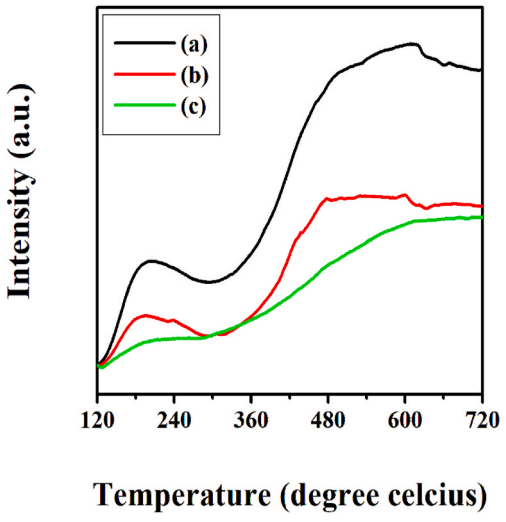

Fig. 16. NH_3-TPD profiles of (a) Co-MCM-48 (20), (b) Co-MCM-48 (40), (c) Co-MCM-48 (80).

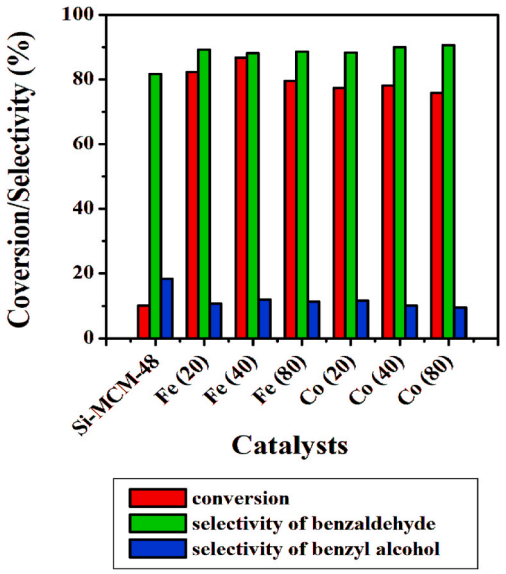

Fig. 17. Effect of metal loading on toluene oxidation. Experimental conditions: reaction time = 8 h, temperature = 353 K, toluene: TBHP = 1: 3, cat = 6 % (w/w) (w.r.t toluene).

4.2. Effect of reaction time on toluene oxidation

Through detailed experimentation involving various catalysts, the reaction conditions for the oxidation of toluene were methodically standardized over a period of 24 h at a precisely controlled temperature of 333 K. At specific time intervals of 2, 4, 6, 8, 12 and 24 h, samples were carefully extracted from the reaction mixture. Among the array of catalysts employed, the iron incorporated MCM-48 material, with an Fe/Si ratio of 40, yielded the most impressive toluene conversion rates. The conversion exhibited a jump from 22.1% to 59.6% as time interval expanded from 2 to 8 h. An interesting observation was made that the reaction reached a state of equilibrium after 8 h, leading to a decline in conversion rates until the culmination of 24 h. In terms of selectivity, benzaldehyde emerged as the preferred product over benzyl alcohol. As the experiment progressed, the selectivity underwent a clear transformation, transitioning from 26.8% to 14.9% for benzyl alcohol, while concurrently expanding from 73.2% to 85.1% for benzaldehyde. This phenomenon indicated that, over time, a greater proportion of benzyl alcohol was effectively converted into benzaldehyde. However, it is noteworthy that the selectivity alteration plateaued as the reaction continued, signifying a marginal shift beyond extended durations. Consequently, based on these insightful findings, it was determined that the catalyst achieved optimal performance for toluene oxidation within an 8-h reaction time (Fig. 18).

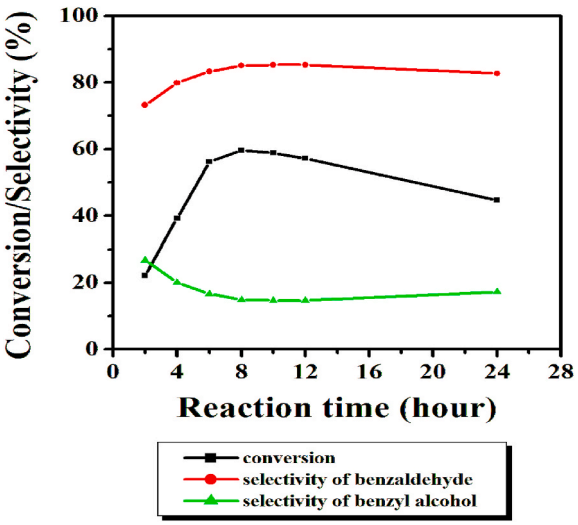

Fig. 18. Effect of reaction time on toluene oxidation. Experimental conditions: temperature = 333 K, toluene: TBHP = 1: 2, cat = 6 % (w/w) (w.r.t toluene), time of collection = 2 h, 4 h, 6 h, 8 h, 12 h and 24 h.

4.3. Effect of temperature on toluene oxidation

An increase in toluene conversion was observed upon elevating the reaction temperature from 298 K to 373 K, as depicted in Fig. 19. A remarkable surge in conversion from 41.4% to 83.3% was recorded as the temperature escalated from 298 K to 353 K. At higher temperatures, the average kinetic energy of the toluene molecules increases, resulting in more effective collisions with the active sites of the catalysts, thereby increasing the toluene conversion rates. Subsequently, a marginal decline in conversion was observed beyond 353 K. This decrease can be attributed to the decomposition of TBHP at higher temperatures, impeding the effective involvement of oxidizing species in the reaction [87]. Consequently, the conversion of toluene is negatively affected. Conversely, with rising temperature, the quantity of benzaldehyde exhibited an increase confirming that benzaldehyde is preferred over benzyl alcohol at high temperature but that increase is sluggish due to decreased availability of oxidizing species thereby inhibiting further oxidation of toluene. Thus, to strike a balance between toluene conversion and benzaldehyde selectivity, the optimal reaction temperature of 353 K was chosen for further oxidation reactions.

4.4. Effect of toluene to TBHP (70% w/v) molar ratio on toluene oxidation

The impact of varying the molar ratio of toluene to TBHP on the reaction was investigated under specific conditions. By varying the

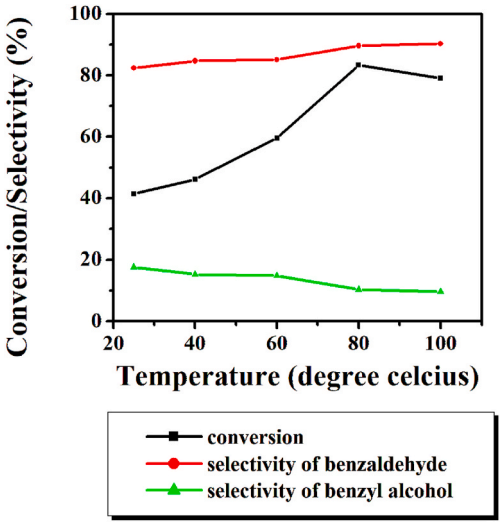

Fig. 19. Effect of temperature on toluene oxidation. Experimental conditions: reaction time = 8 h, toluene: TBHP = 1: 2, cat = 6 % (w/w) (w.r.t toluene).

ratios to 1: 0.5, 1: 1, 1: 2, 1: 3, 1: 4 and 1: 5 at a temperature of 353 K, while deploying 6% (w/w) Fe-MCM-48 (40) as the catalyst, the reaction unfolded in a solvent free surrounding for a calculated stretch of 8 h (Fig. 20). The findings revealed that increasing the toluene: TBHP molar ratio from 1: 0.5 to 1: 3 led to an increase in conversion. However, further increasing the TBHP molar ratio resulted in only a marginal improvement in product formation, likely due to the significant presence of decomposed TBHP on the catalyst's active surface, which hindered access to the mesopores. Moreover, as the amount of TBHP in the reaction mixture increased, the selectivity towards benzaldehyde decreased. This decrease in selectivity could be attributed to the fact that, instead of attaching to the catalyst's active sites, TBHP decomposition occurred, given its excessive abundance in the reaction mixture. The findings conveyed a message that an overabundance of oxidant proved wholly unnecessary in the quest to bolster the catalyst's mettle. Upon comparing both conversion and selectivity, the optimal molar ratio of toluene to TBHP was determined to be 1: 3, yielding an 86.7% toluene conversion rate and 88.1% selectivity to benzaldehyde.

4.5. Effect of catalyst quantity on toluene oxidation

Different masses of iron-loaded MCM-48 catalyst (Si/Fe = 40) were utilized to determine the percentage conversion of toluene and selectivity. The reaction was conducted at 353 K with a toluene to TBHP molar ratio of 1: 3, while varying the weight percentage of the catalyst (w.r.t toluene) from 3% to 15% over an 8-h period. Fig. 21 depicts the influence of catalyst concentration on the oxidation of toluene. Notably, an increase in the amount of catalyst resulted in a rise in toluene conversion and selectivity towards benzaldehyde. This effect can be attributed to a greater involvement of active metal species, leading to enhanced reaction rates. At a catalyst concentration of 6% (w/w), the conversion of toluene reached 86.7% with a corresponding selectivity of 88.1% towards benzaldehyde. However, further increasing the catalyst concentration beyond 6% (w/w) resulted in only minor improvements in product yield, suggesting an optimal threshold where catalyst concentration no longer significantly affects conversion. Conversely, decreasing the catalyst amount from 6% (w/w) to 3% (w/w) led to a decrease in both conversion and selectivity. Therefore, based on these findings, 6% (w/w) was selected as the optimal catalyst amount under the specified reaction conditions.

4.6. Effect of various solvents on toluene oxidation

The influence of different solvents, including ethanol, acetonitrile, acetone, ethyl acetate, chlorobenzene, benzene and cyclohexane, on the conversion and product selectivity during toluene oxidation using Fe-MCM-48 (40) as the catalyst was investigated. The experimental parameters were optimized, including the reaction temperature (353 K), catalyst amount (6% (w/w)) and toluene to TBHP molar ratio of 1: 3. The findings, illustrated in Fig. 22, revealed that all the solvents had a diminishing effect on the oxidation of toluene under similar conditions. Polar protic solvent like ethanol, as well as aprotic solvents such as acetonitrile, acetone, ethyl acetate and chlorobenzene have limited ability to solvate non-polar toluene molecules. However, their solvation of TBHP was relatively effective. Consequently, these solvents did not facilitate the reaction by promoting close proximity between the reactant molecules and the catalyst, which is necessary for successful collisions and interactions. Additionally, these solvents may also potentially get absorbed on the catalyst surface, hindering the access of reactant molecules to the active sites. Similar trends were observed for non-polar solvents like benzene and cyclohexane. As a result, all catalytic studies were conducted under solvent-free conditions.

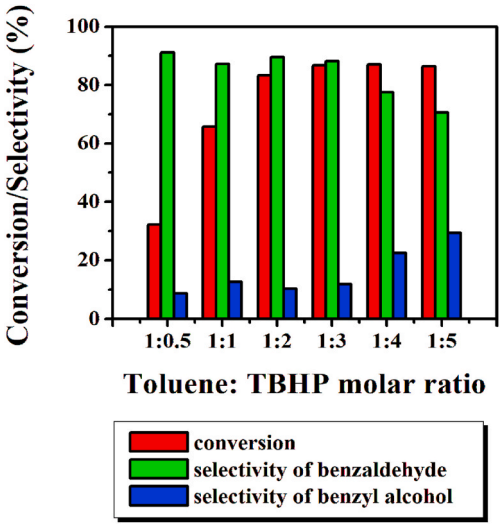

Fig. 20. Effect of toluene to TBHP molar ratio on toluene oxidation. Experimental conditions: reaction time = 8 h, temperature = 353 K, cat = 6 % (w/w) (w.r.t toluene).

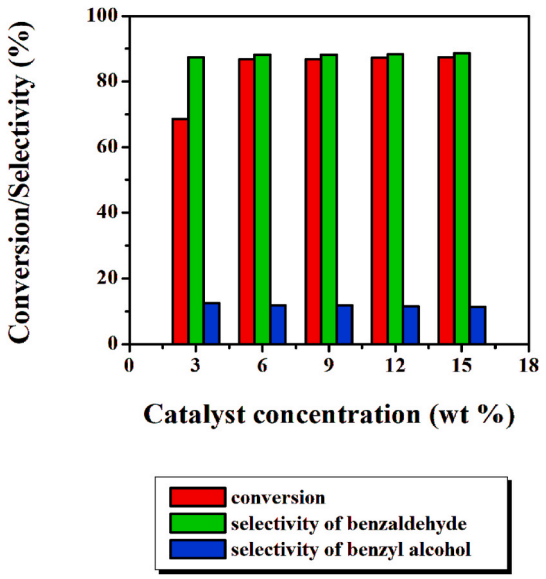

Fig. 21. Effect of catalyst amount on toluene oxidation. Experimental conditions: reaction time = 8 h, temperature = 353 K, toluene: TBHP = 1: 3.

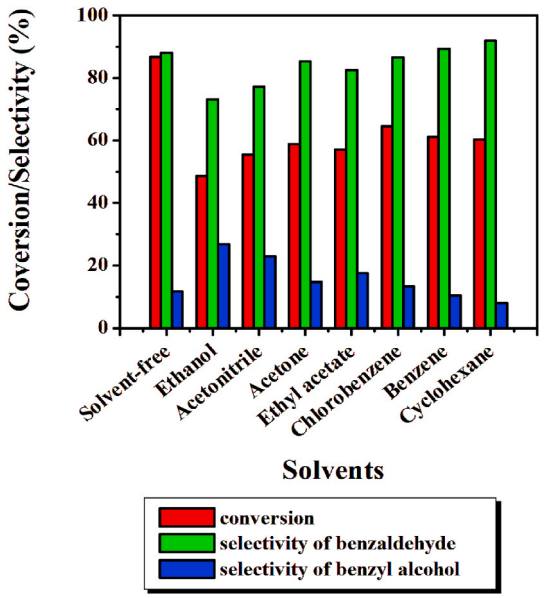

Fig. 22. Effect of different solvents on toluene oxidation. Experimental conditions: reaction time = 8 h, temperature = 353 K, toluene: TBHP = 1: 3, cat = 6 % (w/w) (w.r.t toluene).

4.7. Effect of substituent groups on toluene oxidation

Under the scrupulously optimized reaction conditions, using Fe-MCM-48(40) as the catalyst, we systematically explored various substrates and the comprehensive findings are displayed in Fig. 23. Remarkably, irrespective of the presence of electron-donating or electron-withdrawing substituents in the phenylene ring, the majority of substituted toluene substrates exhibited exemplary selectivity, yielding the corresponding benzaldehyde products.

4.8. Leaching and reusability study of Fe-MCM-48 (40) catalyst

The catalyst Fe-MCM-48 (40) exhibited true heterogeneous behaviour in the oxidation of toluene, with negligible leaching observed during catalyst recycling tests. The catalyst retained its catalytic activity and selectivity across five successive runs,

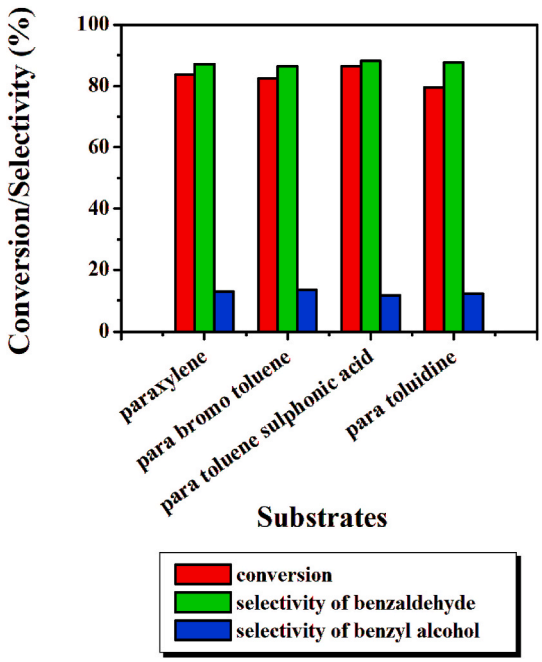

Fig. 23. Effect of substituents on toluene oxidation. Experimental conditions: reaction time = 8 h, temperature = 353 K, toluene: TBHP = 1: 3, cat = 6 % (w/w) (w.r.t toluene).

demonstrating robust performance. XRD and UV–Vis DRS analysis confirmed the structural integrity of the catalyst, with characteristic peaks and metal ions retained within the framework, validating its stability and effectiveness. Please refer to supplementary materials for more details.

5. Conclusion

Through the utilization of a single-step synthesis method, ordered cubic mesoporous materials Si-MCM-48, Fe-MCM-48 (20/40/80) and Co-MCM-48 (20/40/80) were successfully prepared. The systematic characterization of the parent and modified MCM-48 samples using various techniques such as X-ray diffraction (XRD), X-ray photoelectron spectroscopy (XPS), UV–Vis diffuse reflectance spectroscopy (DRS), infrared (IR) spectroscopy, nitrogen adsorption-desorption analysis, scanning electron microscopy with energy dispersive X-ray spectroscopy (SEM-EDX), transmission electron microscopy (TEM), thermal gravimetric analysis (TGA) and NH_3-temperature programmed desorption (TPD) analysis provided an insight into the various physical and chemical properties of the materials. The characterization unveiled mesoporous materials with noteworthy features, encompassing a substantial surface area, precisely defined regular structure and a limited range of pore sizes. Confirmation of heteroatoms' integration into the framework structure of MCM-48 was achieved through thorough combined analysis of results obtained from powder XRD, IR, TGA and EDX techniques. Importantly, the presence of metal cations within the framework position was established by employing XPS and UV–Vis DRS. The mesoporous nature of the samples was confirmed through N_2 adsorption-desorption and TEM analysis. Furthermore, NH_3-TPD analysis confirmed the enhancement of acid site strength of the material with the incorporation of both iron and cobalt into the framework. When subjected to catalytic activity assessment for the oxidation of toluene using *tert*-butyl hydroperoxide (TBHP) as the oxidant it was found that all the iron and cobalt loaded MCM-48 samples showcased remarkable catalytic activity surpassing the performance of Si-MCM-48 yielding a mixture of benzaldehyde and benzyl alcohol as the reaction products. Benzaldehyde selectivity was higher than benzyl alcohol selectivity across all experimental conditions. Noteworthy that Fe-MCM-48 catalysts displayed superior catalytic activity compared to Co-MCM-48 catalysts for toluene oxidation under similar reaction conditions. Utilizing a 6% (w/w) Fe-MCM-48 (40) catalyst and a molar ratio of toluene to TBHP at 1: 3 in a solvent-free environment at 353 K within an 8-h reaction time, an impressive toluene conversion rate of 86.7% was achieved, with a selectivity of 88.1% towards benzaldehyde. The catalyst's heterogeneous nature was verified through leaching and reusability tests, which consistently demonstrated excellent activity even after the fifth run. The employment of iron loaded MCM-48 for catalytic toluene oxidation presents a highly efficient method that addresses the difficulties encountered with traditional homogeneous catalysts.

Funding sources

This research did not receive any specific grant from funding agencies in the public, commercial, or not-for-profit sectors.

Data availability statement

Question	Response
Data Availability Sharing research data helps other researchers evaluate your findings, build on your work and to increase trust in your article. We encourage all our authors to make as much of their data publicly available as reasonably possible. Please note that your response to the following questions regarding the public data availability and the reasons for potentially not making data available will be available alongside your article upon publication. Has data associated with your study been deposited into a publicly available repository?	No
Please select why.	The authors do not have permission to share data

CRediT authorship contribution statement

Arnab Kalita: Writing – review & editing, Writing – original draft, Visualization, Validation, Software, Project administration, Methodology, Investigation, Formal analysis, Data curation, Conceptualization. **Anup Kumar Talukdar:** Writing – review & editing, Supervision, Funding acquisition, Conceptualization.

Declaration of competing interest

The authors declare that they have no known competing financial interests or personal relationships that could have appeared to influence the work reported in this paper.

Acknowledgements

The authors would like to express their sincere gratitude to SAIF, Gauhati University for their invaluable support in providing instrumental facilities. The authors extend their heartfelt appreciation to Dr. Lingaiah Nakka and all the esteemed research scholars of his lab at the Indian Institute of Chemical technology, Hyderabad, for their generous assistance in utilizing the N_2 adsorption-desorption and NH_3-TPD analysis facilities. Additionally, the authors express their sincere gratitude to Dr. Binoy Kumar Saikia at the CSIR-North East Institute of Science and Technology, Jorhat, for his generous support in availing the XPS and TEM analysis facilities. All of their contributions have been truly instrumental in the successful completion of this research work.

Appendix A. Supplementary data

Supplementary data to this article can be found online at https://doi.org/10.1016/j.heliyon.2024.e27296.

References

[1] M.F.H. Zulkifli, N.S.S.L. Hawari, M.T. Latif, H.H. Abd Hamid, A.A.A. Mohtar, W.M.R.W. Idris, N.I.H. Mustaffa, L. Juneng, Volatile organic compounds and their contribution to ground-level ozone formation in a tropical urban environment, Chemosphere 302 (2022) 134852.
[2] V.A. Benignus, Health effects of toluene: a review, Neurotoxicology 2 (3) (1981) 567–588.
[3] C.M. Filley, W. Halliday, B.K. Kleinschmidt-DeMasters, The effects of toluene on the central nervous system, J. Neuropathol. Exp. Neurol. 63 (1) (2004) 1–12.
[4] F. Qu, L. Zhu, K. Yang, Adsorption behaviors of volatile organic compounds (VOCs) on porous clay heterostructures (PCH), J. Hazard Mater. 170 (1) (2009) 7–12.
[5] S. Tian, L. Liu, P. Ning, Phase behavior of tweens/toluene/water microemulsion systems for the solubilization absorption of toluene, J. Solut. Chem. 39 (2010) 457–472.
[6] K.N. Gupta, N.J. Rao, G.K. Agarwal, Gaseous phase adsorption of volatile organic compounds on granular activated carbon, Chem. Eng. Commun. 202 (3) (2015) 384–401.
[7] V.S. Engleman, Updates on choices of appropriate technology for control of VOC emissions, Met. Finish. 108 (11–12) (2010) 305–317.
[8] Z. Huang, X. Gu, Q. Cao, P. Hu, J. Hao, J. Li, X. Tang, Catalytically active single-atom sites fabricated from silver particles, Angew. Chem. 124 (17) (2012) 4274–4279.
[9] R. Muñoz, A.J. Daugulis, M. Hernández, G. Quijano, Recent advances in two-phase partitioning bioreactors for the treatment of volatile organic compounds, Biotechnol. Adv. 30 (6) (2012) 1707–1720.
[10] G.O. Yahaya, Separation of volatile organic compounds (BTEX) from aqueous solutions by a composite organophilic hollow fiber membrane-based pervaporation process, J. Membr. Sci. 319 (1–2) (2008) 82–90.
[11] B. Wang, S. Yao, Y. Peng, Y. Xu, Toluene removal over TiO_2-$BaTiO_3$ catalysts in an atmospheric dielectric barrier discharge, J. Environ. Chem. Eng. 6 (4) (2018) 3819–3826.
[12] J. Van Durme, J. Dewulf, W. Sysmans, C. Leys, H. Van Langenhove, Abatement and degradation pathways of toluene in indoor air by positive corona discharge, Chemosphere 68 (10) (2007) 1821–1829.
[13] Z. Shayegan, C.S. Lee, F. Haghighat, TiO_2 photocatalyst for removal of volatile organic compounds in gas phase–A review, Chem. Eng. J. 334 (2018) 2408–2439.
[14] Z. Zhang, Z. Jiang, W. Shangguan, Low-temperature catalysis for VOCs removal in technology and application: a state-of-the-art review, Catal. Today 264 (2016) 270–278.
[15] E. Kholkina, P. Mäki-Arvela, C. Lozachmeuer, R. Barakov, N. Shcherban, D.Y. Murzin, Prins cyclisation of (–)-isopulegol with benzaldehyde over ZSM-5 based micro-mesoporous catalysts for production of pharmaceuticals, Chin. J. Catal. 40 (11) (2019) 1713–1720.

[16] C. Loch, H. Reusch, I. Ruge, R. Godelmann, T. Pflaum, T. Kuballa, S. Schumacher, D.W. Lachenmeier, Benzaldehyde in cherry flavour as a precursor of benzene formation in beverages, Food Chem. 206 (2016) 74–77.
[17] J.A. Satrio, L.K. Doraiswamy, Production of benzaldehyde: a case study in a possible industrial application of phase-transfer catalysis, Chem. Eng. J. 82 (1–3) (2001) 43–56.
[18] A.M. Malek, A. Barchowsky, R. Bowser, T. Heiman-Patterson, D. Lacomis, S. Rana, A. Youk, E.O. Talbott, Exposure to hazardous air pollutants and the risk of amyotrophic lateral sclerosis, Environ. Pollut. 197 (2015) 181–186.
[19] S. Kausar, N. ul Ain, A.A. Altaf, M. Danish, A. Basit, B. Lal, S. Muhammad, A. Badshah, H.M.K. Javaid, Electrochemical and thermal catalytic studies of Co based molybdenum oxide nanomaterials for CH bond activation, Inorg. Chim. Acta. 517 (2021) 120219.
[20] S.S. Lapari, S. Parham, Oxidation of toluene and hydrogen peroxide catalyzed by Ni (II), Co (II) and Cu (II) Schiff base complexes, Int. J. Eng. Sci. Invent 2 (2013) 62–67.
[21] C. Parmeggiani, C. Matassini, F. Cardona, A step forward towards sustainable aerobic alcohol oxidation: new and revised catalysts based on transition metals on solid supports, Green Chem. 19 (9) (2017) 2030–2050.
[22] Y. Wang, H. Arandiyan, J. Scott, A. Bagheri, H. Dai, R. Amal, Recent advances in ordered meso/macroporous metal oxides for heterogeneous catalysis: a review, J. Mater. Chem. A 5 (19) (2017) 8825–8846.
[23] S. Kausar, A.A. Altaf, M. Hamayun, M. Danish, M. Zubair, S. Naz, S. Muhammad, M. Zaheer, S. Ullah, A. Badshah, Soft template-based bismuth doped zinc oxide nanocomposites for photocatalytic depolymerization of lignin, Inorg. Chim. Acta. 502 (2020) 119390.
[24] S. Kausar, A.A. Altaf, M. Hamayun, N. Rasool, M. Hadait, A. Akhtar, S. Muhammad, A. Badshah, S.A.A. Shah, Z.A. Zakaria, i-propylammonium lead chloride based perovskite photocatalysts for depolymerization of lignin under UV light, Molecules 25 (15) (2020) 3520.
[25] A.A. Altaf, M. Ahmed, M. Hamayun, S. Kausar, M. Waqar, A. Badshah, Titania nano-fibers: a review on synthesis and utilities, Inorg. Chim. Acta. 501 (2020) 119268.
[26] M. Hamza, A.A. Altaf, S. Kausar, S. Murtaza, N. Rasool, R. Gul, A. Badshah, M. Zaheer, S.A. Ali Shah, Z.A. Zakaria, Catalytic removal of alizarin red using chromium manganese oxide nanorods: degradation and kinetic studies, Catalysts 10 (10) (2020) 1150.
[27] B.J. Gallon, R.W. Kojima, R.B. Kaner, P.L. Diaconescu, Palladium nanoparticles supported on polyaniline nanofibers as a semi-heterogeneous catalyst in water, AngewandteChemie International Edition 46 (38) (2007) 7251–7254.
[28] A. Paul, T. Warner, C. John, Green Chemistry: Theory and Practice, vol. 11, New York Oxford Univ Press, Oxford [England, 1998 1394013941.
[29] A.C. Kresge, M.E. Leonowicz, W.J. Roth, J.C. Vartuli, J.S. Beck, Ordered mesoporous molecular sieves synthesized by a liquid-crystal template mechanism, Nature 359 (6397) (1992) 710–712.
[30] K.K. Bania, D. Bharali, B. Viswanathan, R.C. Deka, Enhanced catalytic activity of zeolite encapsulated Fe (III)-Schiff-base complexes for oxidative coupling of 2-napthol, Inorg. Chem. 51 (3) (2012) 1657–1674.
[31] S.K. Das, S.P. Mahanta, K.K. Bania, Oxidative coupling of 2-naphthol by zeolite-Y supported homo and heterometallic trinuclear acetate clusters, RSC Adv. 4 (93) (2014) 51496–51509.
[32] W. Zhao, Q. Li, L. Wang, J. Chu, J. Qu, S. Li, T. Qi, Synthesis of high quality MCM-48 with binary Cationic− nonionic surfactants, Langmuir 26 (10) (2010) 6982–6988.
[33] P.J. Branton, P.G. Hall, K.S. Sing, H. Reichert, F. Schüth, K.K. Unger, Physisorption of argon, nitrogen and oxygen by MCM-41, a model mesoporous adsorbent, J. Chem. Soc., Faraday Trans. 90 (19) (1994) 2965–2967.
[34] J.W. Lee, D.L. Cho, W.G. Shim, H. Moon, Application of mesoporous MCM-48 and SBA-15 materials for the separation of biochemicals dissolved in aqueous solution, Kor. J. Chem. Eng. 21 (2004) 246–251.
[35] Q. Huang, M. Eić, H. Xiao, S. Kaliaguine, Characterization of the diffusion path in micro-and meso-porous materials from ZLC analysis, Adsorption 16 (2010) 531–539.
[36] P.A. Russo, M.R. Carrott, P.J.M. Carrott, J.M. Lopes, F.R. Ribeiro, J. Rocha, Structure and catalytic activity of Al-MCM-48 materials synthesised at room temperature: influence of the aluminium source and calcination conditions, Microporous Mesoporous Mater. 114 (1–3) (2008) 293–302.
[37] Q. Zhao, X. Zhou, M. Ji, H. Ding, T. Jiang, C. Li, H. Yin, Stability and textural properties of cobalt incorporated MCM-48 mesoporous molecular sieve, Appl. Surf. Sci. 257 (7) (2011) 2436–2442.
[38] T. Kawabata, Y. Ohishi, S. Itsuki, N. Fujisaki, T. Shishido, K. Takaki, Q. Zhang, Y. Wang, K. Takehira, Iron-containing MCM-41 catalysts for Baeyer–Villiger oxidation of ketones using molecular oxygen and benzaldehyde, J. Mol. Catal. Chem. 236 (1–2) (2005) 99–106.
[39] D.H. Koo, M. Kim, S. Chang, WO3 nanoparticles on MCM-48 as a highly selective and versatile heterogeneous catalyst for the oxidation of olefins, sulfides and cyclic ketones, Org. Lett. 7 (22) (2005) 5015–5018.
[40] M. Nandi, A.K. Talukdar, Vanadia loaded hierarchical ZSM-5 zeolite: a promising catalyst for epoxidation of cyclohexene under solvent free condition, J. Porous Mater. 23 (2016) 1143–1154.
[41] K.K. Bania, G.V. Karunakar, L. Satyanarayana, Oxidative coupling of 2-naphthol to (R)/(S)-BINOL by MCM-41 supported Mn-chiral Schiff base complexes, RSC Adv. 5 (42) (2015) 33185–33198.
[42] K. Moller, T. Bein, Inclusion chemistry in periodic mesoporous hosts, Chem. Mater. 10 (10) (1998) 2950–2963.
[43] B. Kalita, P. Phukan, A.K. Talukdar, Oxidation of anisole over MCM-48 materials modified by incorporation of transition and inner transition metals, Catal. Sci. Technol. 2 (11) (2012) 2341–2350.
[44] D.R. Das, A.K. Talukdar, Facile synthesis of titanium-loaded MCM-48 as an efficient heterogeneous catalyst for selective oxidation of aniline to azoxybenzene, ChemistrySelect 2 (28) (2017) 8983–8989.
[45] W. Zhao, Y. Luo, P. Deng, Q. Li, Synthesis of Fe-MCM-48 and its catalytic performance in phenol hydroxylation, Catal. Lett. 73 (2001) 199–202.
[46] V. Parvulescu, C. Anastasescu, B.L. Su, Bimetallic Ru-(Cr, Ni, or Cu) and La-(Co or Mn) incorporated MCM-41 molecular sieves as catalysts for oxidation of aromatic hydrocarbons, J. Mol. Catal. Chem. 211 (1–2) (2004) 143–148.
[47] F.G. Nogueira, J.H. Lopes, A.C. Silva, R.M. Lago, J.D. Fabris, L.C. Oliveira, Catalysts based on clay and iron oxide for oxidation of toluene, Appl. Clay Sci. 51 (3) (2011) 385–389.
[48] Y. Xia, M. Lin, D. Ren, Y. Li, F. Hu, W. Chen, Preparation of high surface area mesoporous nickel oxides and catalytic oxidation of toluene and formaldehyde, J. Porous Mater. 24 (2017) 621–629.
[49] Y. Qin, Z. Qu, C. Dong, Y. Wang, N. Huang, Highly catalytic activity of Mn/SBA-15 catalysts for toluene combustion improved by adjusting the morphology of supports, J. Environ. Sci. 76 (2019) 208–216.
[50] X. Fu, Y. Liu, W. Yao, Z. Wu, One-step synthesis of bimetallic Pt-Pd/MCM-41 mesoporous materials with superior catalytic performance for toluene oxidation, Catal. Commun. 83 (2016) 22–26.
[51] F. Benais-Hamidi, L. Chérif-Aouali, S. Siffert, R. Cousin, A. Bengueddach, Total oxidation of toluene over gold supported on mesoporous ferrisilicates materials, Int. J. Environ. Pollut. 58 (3) (2015) 187–196.
[52] D. Romero, D. Chlala, M. Labaki, S. Royer, J.P. Bellat, I. Bezverkhyy, J.M. Giraudon, J.F. Lamonier, Removal of toluene over NaX zeolite exchanged with Cu^{2+}, Catalysts 5 (3) (2015) 1479–1497.
[53] K. Bendahou, L. Cherif, S. Siffert, H.L. Tidahy, H. Benaissa, A. Aboukais, The effect of the use of lanthanum-doped mesoporous SBA-15 on the performance of Pt/SBA-15 and Pd/SBA-15 catalysts for total oxidation of toluene, Appl. Catal. Gen. 351 (1) (2008) 82–87.
[54] H.W. Ryu, M.Y. Song, J.S. Park, J.M. Kim, S.C. Jung, J. Song, B.J. Kim, Y.K. Park, Removal of toluene using ozone at room temperature over mesoporous Mn/Al_2O_3 catalysts, Environ. Res. 172 (2019) 649–657.
[55] S. Narayanan, J.J. Vijaya, S. Sivasanker, L.J. Kennedy, P. Kathirgamanathan, R. Azhagu Raj, Synthesis of hierarchical ZSM-5 hexagonal cubes and their catalytic activity in the solvent-free selective oxidation of toluene, J. Porous Mater. 22 (2015) 907–918.
[56] S. Peta, T. Zhang, V. Dubovoy, K. Koh, M. Hu, X. Wang, T. Asefa, Facile synthesis of efficient and selective Ti-containing mesoporous silica catalysts for toluene oxidation, Mol. Catal. 444 (2018) 34–41.

[57] N. Qiao, Y. Li, N. Li, X. Zhang, J. Cheng, Z. Hao, High performance Pd catalysts supported on bimodal mesopore silica for the catalytic oxidation of toluene, Chin. J. Catal. 36 (10) (2015) 1686–1693.
[58] H. Huang, C. Zhang, L. Wang, G. Li, L. Song, G. Li, S. Tang, X. Li, Promotional effect of HZSM-5 on the catalytic oxidation of toluene over MnOx/HZSM-5 catalysts, Catal. Sci. Technol. 6 (12) (2016) 4260–4270.
[59] A. Boro, A.K. Talukdar, Phenol hydroxylation over Fe and Co-loaded mesoporous MCM-48, J. Porous Mater. 26 (2019) 1185–1196.
[60] A.A. Romero, M.D. Alba, W. Zhou, J. Klinowski, Synthesis and characterization of the mesoporous silicate molecular sieve MCM-48, J. Phys. Chem. B 101 (27) (1997) 5294–5300.
[61] Y. Shao, L. Wang, J. Zhang, M. Anpo, Synthesis of hydrothermally stable and long-range ordered Ce-MCM-48 and Fe-MCM-48 materials, J. Phys. Chem. B 109 (44) (2005) 20835–20841.
[62] D.R. Das, P. Kalita, A.K. Talukdar, Ti/Cr incorporated mesoporous MCM-48 for oxidation of styrene to benzaldehyde, J. Porous Mater. 27 (2020) 893–903.
[63] P. Kalita, N.M. Gupta, R. Kumar, Synergistic role of acid sites in the Ce-enhanced activity of mesoporous Ce–Al-MCM-41 catalysts in alkylation reactions: FTIR and TPD-ammonia studies, J. Catal. 245 (2) (2007) 338–347.
[64] Y. Liu, Hydrocracking of polyethylene to jet fuel range hydrocarbons over bifunctional catalysts containing Pt-and Al-modified MCM-48, Reactions 1 (2) (2020) 195–209.
[65] P. Trongjitraksa, A. Jantharasuk, W. Jareewatchara, Y. Klinthongchai, B. Jongsomjit, P. Praserthdam, Enhancement of the thermal stability for MCM-48 with incorporation of different metals, Microporous Mesoporous Mater. 354 (2023) 112556.
[66] Y. Yan, X. Wu, H. Zhang, Catalytic wet peroxide oxidation of phenol over Fe_2O_3/MCM-41 in a fixed bed reactor, Sep. Purif. Technol. 171 (2016) 52–61.
[67] Y. Ling, H. Liu, B. Li, B. Zhang, Y. Wu, H. Hu, D. Yu, S. Huang, Efficient photocatalytic ozonation of azithromycin by three-dimensional g-C_3N_4 nanosheet loaded magnetic Fe-MCM-48 under simulated solar light, Appl. Catal. B Environ. 324 (2023) 122208.
[68] A. De Stefanis, S. Kaciulis, L. Pandolfi, Preparation and characterization of Fe-MCM-41 catalysts employed in the degradation of plastic materials, Microporous Mesoporous Mater. 99 (1–2) (2007) 140–148.
[69] F. Yang, S. Zhou, H. Wang, S. Long, X. Liu, Y. Kong, A metal-assisted templating route (S0M+ I −) for fabricating thin-layer CoO covered on the channel of nanospherical-HMS with improved catalytic properties, Dalton Trans. 45 (2016) 6371–6382.
[70] Y. Jiang, X. Li, T. Wang, C. Wang, Enhanced electrocatalytic oxygen evolution of α-$Co(OH)_2$ nanosheets on carbon nanotube/polyimide films, Nanoscale 8 (2016) 9667–9675.
[71] S. Zhou, C. Song, W. Kong, B. Wang, Y. Kong, Effects of synergetic effect between Co and γ-Fe_2O_3 in confined silica matrix of MCM-41 on the formation of free radicals for the advanced oxidation technology, Appl. Surf. Sci. 527 (2020) 146853.
[72] P. Kuśtrowski, L. Chmielarz, R. Dziembaj, P. Cool, E.F. Vansant, Modification of MCM-48-, SBA-15-, MCF- and MSU-type mesoporous silicas with transition metal oxides using the molecular designed dispersion method, J. Phys. Chem. B 109 (23) (2005) 11552–11558.
[73] S. Madadi, L. Charbonneau, J.Y. Bergeron, S. Kaliaguine, Aerobic epoxidation of limonene using cobalt substituted mesoporous SBA-16 Part 1: optimization via Response Surface Methodology (RSM), Appl. Catal. B Environ. 260 (2020) 118049.
[74] H. Ma, J. Xu, C. Chen, Q. Zhang, J. Ning, H. Miao, L. Zhou, X. Li, Catalytic aerobic oxidation of ethylbenzene over Co/SBA-15, Catal. Lett. 113 (2007) 104–108.
[75] Y. Dong, X. Zhan, X. Niu, J. Li, F. Yuan, Y. Zhu, H. Fu, Facile synthesis of Co-SBA-16 mesoporous molecular sieves with EISA method and their applications for hydroxylation of benzene, Microporous Mesoporous Mater. 185 (2014) 97–106.
[76] L.H. Little, A.V. Kiselev, V.I. Lygin, Infrared Spectra of Adsorbed Species, No Title, 1966.
[77] Z.H.A.N. Wangcheng, L.U. Guanzhong, G.U.O. Yanglong, G.U.O. Yun, W.A.N.G. Yanqin, W.A.N.G. Yunsong, Z. Zhang, L.I.U. Xiaohui, Synthesis of cerium-doped MCM-48 molecular sieves and its catalytic performance for selective oxidation of cyclohexane, J. Rare Earths 26 (4) (2008) 515–522.
[78] A.A. Romero, M.D. Alba, J. Klinowski, Aluminosilicate mesoporous molecular sieve MCM-48, J. Phys. Chem. B 102 (1) (1998) 123–128.
[79] F.L. Galeener, A.E. Geissberger, Vibrational dynamics in Si 30-substituted vitreous SiO_2, Phys. Rev. B 27 (10) (1983) 6199.
[80] S. Gai, P. Yang, D. Wang, C. Li, N. Niu, F. He, M. Zhang, J. Lin, Luminescence functionalization of MCM-48 by YVO 4: Eu^{3+} for controlled drug delivery, RSC Adv. 2 (8) (2012) 3281–3287.
[81] M.S. Morey, S. O'Brien, S. Schwarz, G.D. Stucky, Hydrothermal and postsynthesis surface modification of cubic, MCM-48 and ultralarge pore SBA-15 mesoporous silica with titanium, Chem. Mater. 12 (4) (2000) 898–911.
[82] S. Gómez, O. Giraldo, L.J. Garcés, J. Villegas, S.L. Suib, New synthetic route for the incorporation of manganese species into the pores of MCM-48, Chem. Mater. 16 (12) (2004) 2411–2417.
[83] L. Wang, L. Xing, J. Liu, T. Qi, S. Zhang, Y. Ma, P. Ning, Construction of lattice-confined Co-MCM-48 for boosting sulfite oxidation in wet desulfuration, Chem. Eng. J. 407 (2021) 127210.
[84] L. Rivoira, J. Juárez, M.L. Martínez, A. Beltramone, Iron-modified mesoporous materials as catalysts for ODS of sulfur compounds, Catal. Today 349 (2020) 98–105.
[85] H. Subramanian, E.G. Nettleton, S. Budhi, R.T. Koodali, Baeyer–Villiger oxidation of cyclic ketones using Fe containing MCM-48 cubic mesoporous materials, J. Mol. Catal. Chem. 330 (1–2) (2010) 66–72.
[86] X. Li, W. Chen, Y. Tang, L. Li, Relationship between the structure of Fe-MCM-48 and its activity in catalytic ozonation for diclofenac mineralization, Chemosphere 206 (2018) 615–621.
[87] W. Li, Y. Xu, J. Wang, Z. Zhai, Z. Yan, Y. Yang, Selective oxidation of 4-tert-butyltoluene to 4-tert-butylbenzaldehyde over Co/MCM-41, Catal. Lett. 119 (2007) 327–331.
[88] A.V. Shijina, N.K. Renuka, Hydrogen peroxide oxidation of toluene over V/Al systems, React. Kinet. Catal. Lett. 94 (2008) 261–270.
[89] B. Lu, N. Cai, J. Sun, X. Wang, X. Li, J. Zhao, Q. Cai, Solvent-free oxidation of toluene in an ionic liquid with H_2O_2 as oxidant, Chem. Eng. J. 225 (2013) 266–270.
[90] W. Zhou, K. Huang, M. Cao, F.A. Sun, M. He, Z. Chen, Selective oxidation of toluene to benzaldehyde in liquid phase over CoAl oxides prepared from hydrotalcite-like precursors, React. Kinet. Mech. Catal. 115 (2015) 341–353.
[91] H. Shoukat, A.A. Altaf, M. Hamayun, S. Ullah, S. Kausar, M. Hamza, S. Muhammad, A. Badshah, N. Rasool, M. Imran, Catalytic oxidation of toluene into benzaldehyde and benzyl alcohol using molybdenum-incorporated manganese oxide nanomaterials, ACS Omega 6 (30) (2021) 19606–19615.
[92] A.A. Verberckmoes, B.M. Weckhuysen, R.A. Schoonheydt, Spectroscopy and coordination chemistry of cobalt in molecular sieves, Microporous Mesoporous Mater. 22 (1–3) (1998) 165–178.
[93] A. Vinu, J. Dědeček, V. Murugesan, M. Hartmann, Synthesis and characterization of CoSBA-1 cubic mesoporous molecular sieves, Chem. Mater. 14 (6) (2002) 2433–2435.